Check for updates

View Article Online
View Journal

PCCP
Physical Chemistry Chemical Physics

Accepted Manuscript

This article can be cited before page numbers have been issued, to do this please use: M. Idrees, H. U. Din, S. U. Reman, M. Shafiq, Y. Saeed, B. Dinh, C. Nguyen and B. Amin, *Phys. Chem. Chem. Phys.*, 2020, DOI: 10.1039/D0CP01264E.

This is an Accepted Manuscript, which has been through the Royal Society of Chemistry peer review process and has been accepted for publication.

Accepted Manuscripts are published online shortly after acceptance, before technical editing, formatting and proof reading. Using this free service, authors can make their results available to the community, in citable form, before we publish the edited article. We will replace this Accepted Manuscript with the edited and formatted Advance Article as soon as it is available.

You can find more information about Accepted Manuscripts in the Information for Authors.

Please note that technical editing may introduce minor changes to the text and/or graphics, which may alter content. The journal's standard Terms & Conditions and the Ethical guidelines still apply. In no event shall the Royal Society of Chemistry be held responsible for any errors or omissions in this Accepted Manuscript or any consequences arising from the use of any information it contains.

ROYAL SOCIETY OF CHEMISTRY

rsc.li/pccp

View Article Online
DOI: 10.1039/D0CP01264E

Journal Name

ARTICLE TYPE

Cite this: DOI: 10.1039/xxxxxxxxxx

Electronic properties and enhanced photocatalytic performance of van der Waals Heterostructures of ZnO and Janus transition metal dichalcogenides

M. Idrees[1], H. U-Din[1], Shafiq Ur Rehman[2], M. Shafiq[3], Yasir Saeed[3], H. D. Bui[4], Chuong V. Nguyen[4†], Bin Amin[3†]

Received Date
Accepted Date

DOI: 10.1039/xxxxxxxxxx

www.rsc.org/journalname

Vertical stacking of two-dimensional materials into layered van der Waals heterostructures are recently considered as promising candidate for photocatalytic and optoelectronic devices because they can combine advantages of the individual 2D materials. Janus transition metals dichalcogenides (JTMDCs) have emerged as an appealing photocatalytic material due to the desirable electronic properties. Hence, in this work, we systematically investigate the geometric features, electronic properties, charge density difference, work function, band alignment and photocatalytic properties of ZnO-JTMDCs heterostructures using first-principles calculations. Due to the different kinds of chalcogen atoms on both sides of JTMDCs monolayers, two different possible stacking patterns of ZnO-JTMDCs heterostructures have been constructed and considered. We find that all these stacking patterns of ZnO-JTMDCs heterostructures are dynamically and energetically feasible. Moreover, both ZnO-MoSSe and ZnO-WSSe heterostructures exhibit indirect band gap semiconductors and present the type-I and type-II band alignments for Model-I and Model-II, respectively. The Rashba spin polarization of ZnO-WSSe heterostructure for model-I is greater than that in the others. Furthermore, valence(conduction) band edge potentials are calculated to understand the photocatalytic behavior of these systems. Energetically favorable band edge positions in ZnO-Janus heterostucturs make them suitable for water splitting at zero pH. We found that the ZnO-Janus heterostructure are promising candidates for water splitting with conduction and valence band edges positioned just outside of the redox interval.

1 Introduction

Hydrogen is known to be a pollution-free fuel in the fuel cell technology, however, the process of hydrogen production is so not clean and pollution free[1–5]. Recently, photocatalytic water splitting is an alternative way for producing hydrogen, where semiconducting materials with desired valence and conduction band energy are considered as potential candidate for the conversion of solar light into hydrogen[6–9]. The overall water splitting into hydrogen and oxygen gases is achieved since irradiating light on the semiconductor generate electrons (holes) in the conduction (valence) band reduce(oxidize) water molecules [10,11]. In addition, one of the most important requirements for a semiconductor, which is suitable for photocaltalytic water splitting reactions is the positions of its band edges. In the other word, the conduction band should be higher than the redox potential of H^+/H_2 (0 eV), while the valence band should be smaller that the redox potential of O_2/H_20 (1.23 eV). It demonstrates that the band gap value of the desired semiconductors should be larger than 1.23 eV.

Up to date, two-dimensional (2D) materials have been widely emerged due to their wide range of applications in catalysis[12], electrochemical energy storage[13,14], photocatalysis[15], electronics[16,17], optoelectronics[18,19], spintronics[20–22] and photonic nanodevices[23]. Among these, transition metal dichalcogenides (TMDCs) have received considerable interest because of their fascinating properties[24]. However, the TMDCs monolayers show some disadvantages, such as large effective masses, weak dielectric screening, and strong excitonic effect[25], leading to the fast rate of the recombination of photongenerated electron and hole. The short lifetime for electron-hole pair leads to an extremely

[1] Department of Physics, Hazara University, Mansehra 21300, Pakistan
[2] College of Physics and Optoelectronic Engineering, Shenzhen University, Guangdong 518060, China
[3] Abbottabad Uniersity of Science and Technology, Abbottabad 22010, Pakistan
[4] Department of Materials Science and Engineering, Le Quy Don Technical University, Ha Noi 100000, Vietnam.
† To whom correspondence should be addressed. Email: chuongnguyen11@gmail.com; binukhn@gmail.com

Published on 20 April 2020. Downloaded by Chalmers Tekniska Hogskola on 4/20/2020 6:31:51 AM.

Physical Chemistry Chemical Physics Accepted Manuscript

View Article Online
DOI: 10.1039/D0CP01264E

Published on 20 April 2020. Downloaded by Chalmers Tekniska Hogskola on 4/20/2020 6:31:51 AM.

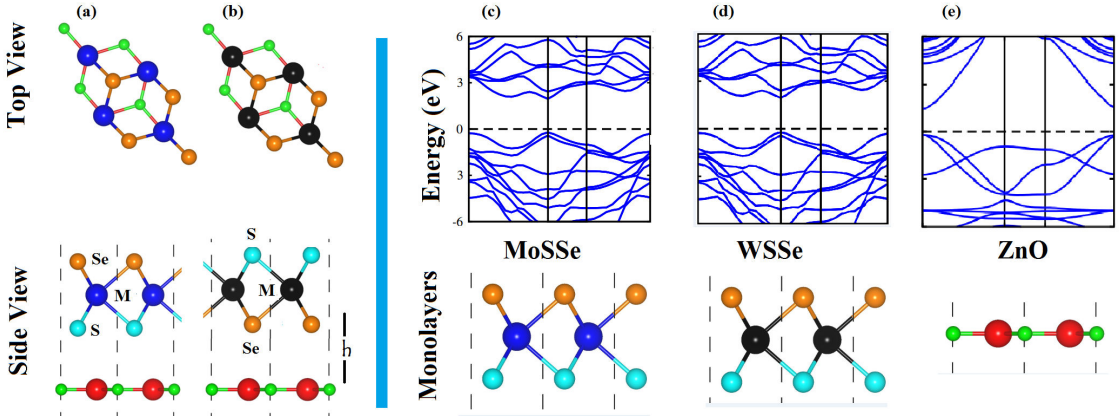

Fig. 1 (a, b) The most favorable staking configurations in Model-I and Model-II of the ZnO-MSSe (M = Mo, W) heterostructures. Band structure and side view of (c) MoSSe, (e) WSSe and ZnO monolayers, respectively. Red and green balls represent the Zn and O atoms, respectively.

low quantum efficiency, thus the device's performance is dramatically impeded. In order to break this limitation in 2D TMDCs, many common strategies have been developed, such as applying electric field[26], strain engineering[27], layer stackings[28,29] and controlling their composition[30]. Among these, stacking different 2D materials into layered vdW heterostructures are considered as a practical way for designing next-generation applications, ranging from nanoelectronics to optoelectronics and photonics, such as tunneling transistors[31], solar cells[32] and bipolar transistors[33]. Especially, the formation of type-II band alignment in the layered vdW heterostructures is capable to modulate interlayer transition energy and responsible for charge separation, hence intensively uses in designing advanced optoelectronic devices.

Recently, polar Janus TMDCs MXY (M = Mo, W; X/Y = S, Se, Te) monolayers can be obtained in experiments either by sulfurization strategy of monolayer $MoSe_2$ or selenization one of monolayer MoS_2[34]. One can observe that a large Rashba spin splitting, originating from the atomic radius and electronegativity differences of the X and Y chalcogen elements in Janus TMDCs MXY makes them promising for futuristic spintronic devices. For instance, Xia et. al.[35] from first-principles calculations investigated electronic and photocatalystic features of different kinds of Janus TMDCs MXY and demonstrated that they are promising candidate for highly efficient photocatalysts. At the same time, a sp^2 graphene-like ZnO monolayer is gaining enormous interest from both theoretical and experimental scientific communities[36]. The fascinating physical and chemical properties of ZnO monolayer, such as chemical bonding, large exciton binding energy make it fascinating material for transparent electronics, solar cells and gas sensor[37].

The vdW heterostructures between Janus TMDCs MXY and other 2D materials, such as MXY-GeC[38], MXY-graphene[39,40], MXY-GaN[41,42] have been constructed and considered as a powerful strategy to enhance the electronic and photocatalytic features of 2D materials. For instance, Din et al.[38] designed the MSSe-GeC (M = Mo, W) heterostructures and investigated their electronic, and photocatalytic properties. They also predicted that these vdW heterostructures can be used for designing next-generation electronic devices and photocatalytic water splitting. Yin et al. studied the effect of strain on the photocatalytic properties of Janus MoSSe/nitrides heterostructure[42]. Xu et. al investigated the Janus MoSSe/GaN vdW heterobilayers for band alignment transition and optical properties[41]. Cavalcante et al. studied the plasmons in Janus MoSSe-Graphene Based van der Waals Heterostructures[40], whereas by first principles calculations, Pham et al. investigated the electronic properties and Schottky barrier in vertically stacked graphene/Janus MoSeS heterostructure under electric field[39]. However, to our best knowledge, the electronic properties and photocatalytic performance of the vdW heterostructures between ZnO and Janus MSSe (M = Mo, W) have not yet previously been investigated. Based on above interesting phenomena, it is extremely interesting to check whether the vdW heterostructures based on ZnO and Janus TMDCs MXY could be considered as promising candidate for photocatalytic and optoelectronic devices. Therefore, in this work, using first principle calculations, we have systematically investigated the stabilities, electronic structures, induced SOC Rashba spin spilitting, interlayer charge transfer, work function and photocatalytic performance of these heterostructures.

2 Computational details

All our calculations are based on the density functional theory (DFT)[43] in conjunction with the projector-augmented-wave (PAW) potential as implemented in the Vienna ab initio simulation package (VASP)[44,45]. The Perdew-Burke-Ernzerhof generalized gradient approximation (GGA)[46] with the approach of Grimme (DFT-D2)[47] is adopted to correct the weak Van der Waals like interaction. The cutoff energy for the plane wave basis set is 500 eV, and the first Brillouin zone is sampled with Monkhorst-Pack grid of $12\times12\times1$. All atomic positions were fully relaxed until the force is less than 0.01 eV/Å and the criterion for the total energy conversion is set to 10^{-5} eV. A vacuum space of 25 Å along he z direction is used to decouple possible periodic interactions. Since the PBE functional and GGA approach usually underestimate the band gaps of semiconductors [40], the screened hybrid Heyd-Scuseria-Ernzerhof (HSE06) functional[48] has been employed to get accurate electronic structures.

The effect of spin-orbit coupling (SOC) is significant for Janus

Physical Chemistry Chemical Physics Accepted Manuscript

This journal is © The Royal Society of Chemistry [year]

View Article Online
DOI: 10.1039/D0CP01264E

Published on 20 April 2020. Downloaded by Chalmers Tekniska Hogskola on 4/20/2020 6:31:51 AM.

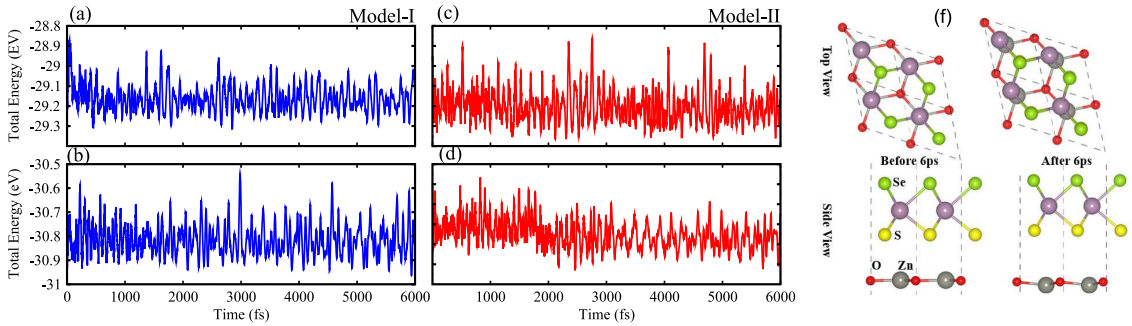

Fig. 2 Thermal stabilities of model-I (a) MoSSe-ZnO (b) WSSe-ZnO; model-II (c) MoSSe-ZnO and (d) WSSe-ZnO van der Waals heterostructures. (f) is the atomic structure of ZnO/MoSSe for Model-I before and after heating of 6 ps.

monolayers and hence is taken into account in all calculations, incorporated by a second variational method [56], which uses scalar-relativistic basis, based on the reduction of original basis. In variational method, the scalar relativistic part of Hamiltonian is diagonlized in scalar relativistic basis and the calculated eigen functions are then used to construct the full Hamiltonian matrix including SOC and may be written as: $\psi = \varepsilon\psi + H\psi$, here H$\psi$ represents for the spin-orbit Hamiltonian.

Ab initio molecular dynamics simulations (AIMD) [49] is used to investigate the thermal stabilities of ZnO-janus van der Waals heterostructures. AIMD simulations are performed through Nose-thermostat algorithm at temperature of 300 K for total 6 ps with a time interval of 1 fs.

3 Results and discussion

We first check the optimized lattice constant and bond-length values for ZnO and Janus TMDCs, as listed in Table 1. These results are in good agreement with previous reports [50,51], indicating the reliability of our calculated method. The ZnO, MoSSe and WSSe monolayers are direct band gap semiconducors with the band gap values of 2.06 eV, 2.07 eV and 3.10 eV, respectively, as illustrated in Fig. 1. We can find from Table 1 that Janus MXY and ZnO monolayers have the same lattice constants, resulting in a small lattice mismatch of the ZnO-Janus MXY heterostructures. The lattice mismatch in ZnO-MoSSe and ZnO-WSSe are 0.9% and 0.6%, respectively, demonstrating the they can be easily fabricated for practical applications. The atomic structures of ZnO-Janus MXY heterostructures are depicted in Fig. 1(a,b). Based on different chalcogen atoms in Janus monolayer two modeled heterostructures each with six favorable high-symmetry stacking sequences of atoms are investigated (see Ref. [50] for details). Top and side views of favorable and most stable staking is plotted, in which the Mo(W) atom is in the top of Zn atom while S, Se and O is in the hexagonal side for both models. Herein, h stands for the interlayer distance between ZnO and Janus MXY monolayers in the corresponding heterostructures. Due to different kinds of chalcogen atoms in both sides of Janus MSSe monolayer, there are two stacking models of ZnO-Janus MSSe heterostructures, namely Model-I and Model-II, which represent the ZnO-SMSe and ZnO-SeMS heterostructures, respectively.

The binding energy is also calculated in order to check the structural stability and to find the most stable stacking configurations for both model-I and model-II as follows: $E_b = E_{total} - E_{ZnO} - E_{JMXY}$, where E_{total}, E_{ZnO}, and E_{JMXY} represent the energy of the whole system, the ZnO and Janus MXY monolayers, respectively. The results of the binding energies in all stacking configurations of ZnO-Janus MXY heterostructures are listed in Table 2. We can find that the ZnO-Janus MXY heterostructures for their different stacking configurations are energetically favorable and thus they can be easily fabricated in experiments for practical productions. One can also find from Tab. 2 that all these heterostructures are characterized by the weak vdW interactions, dominating between ZnO and Janus MXY monoalyers. Moreover, it is clear that the smaller value of binding energy means a stronger interface binding and therefore a more stable system. Configuration of the shortest interlayer distance in Fig. 2 and more negative value of binding energy than the other is chosen for our work in both models, as listed in Tab. 2.

Table 1 Lattice constant (Å), bond lengths ($M-X$), band gap (E_g-HSE), conduction and valence band edges of MoSSe, WSSe and ZnO monolayers.

monolayers	MoSSe	WSSe	ZnO
a (Å)	3.25	3.26	3.29
Mo(W)–S/Zn–O (Å)	2.51	2.51	1.88
Mo(W)–Se (Å)	2.50	2.50	-
E_g-HSE (eV)	2.06	2.07	3.10
E_{VB} (eV)	1.77	1.95	2.47
E_{CB} (eV)	-0.29	-0.12	-0.63

Moreover, it is clear that the thermal stability is an important indicator for the performance assessment of supported 2D materials. Therefore, we further perform *ab initio* molecular dynamics (AIMD) simulations to check the structural distortion and stability of ZnO-MoSSe and ZnO-WSSe heterostructures. We can see from Figure 2 that the ZnO-MoSSe and ZnO-WSSe heterostructures retain their geometries without any structural distortion after 6 ps. These system shows small variations in the total energies of ZnO-Janus MXY vdW heterostructures, which are thermally stable at the temperature room (300 K).

Band structures of Model-I of the ZnO-Janus MXY heterostructure obtained from PBE, HSE06 and PBE-SOC are depicted in Figure 3. Our results show that the Model-I of the ZnO-MoSSe and ZnO-WSSe vdW heterostructures without the SOC effect ex-

Physical Chemistry Chemical Physics Accepted Manuscript

View Article Online
DOI: 10.1039/D0CP01264E

Published on 20 April 2020. Downloaded by Chalmers Tekniska Hogskola on 4/20/2020 6:31:51 AM.

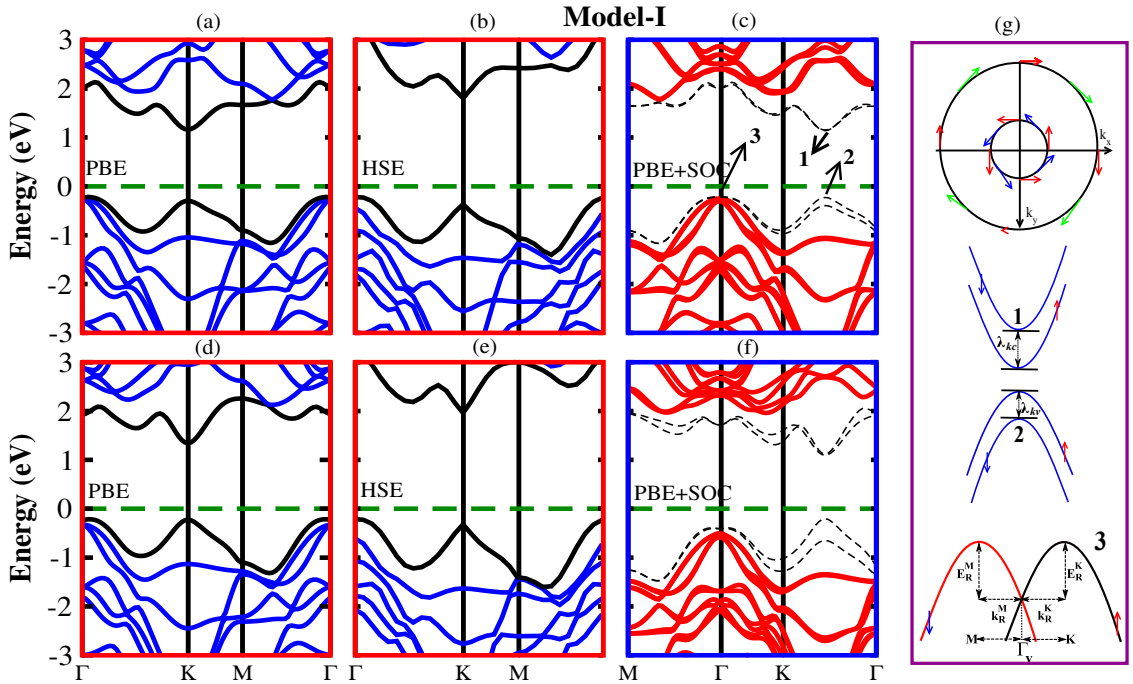

Fig. 3 Model-I: band structure of MoSSe-ZnO (a, b and c) and WSSe-ZnO (d, e and f) van der Waals heterostructures (g) Schematic of spin texture of two bands around Γ_v, and the encircled numbers(1, 2 and 3) represent the magnified view of valence band, conduction band-splitting at K-point and Rashba spin splitting around Γ_v

hibit indirect band gap semiconductors with the VBM at the Γ-point and the CBM at the K-point, as shown in Fig. 3(a,b) and Fig. 3(d,e). The band gap values of the ZnO-MoSSe and ZnO-WSSe vdW heterostructures given by PBE/HSE, respectively, are 1.40 eV/2.0 eV and 1.53 eV/2.1 eV, as listed in Table. 2. Interestingly, including the SOC effect in PBE calculations shifts the CBM from K-point to $\Gamma - K$-point and splits the band structure of ZnO-MoSSe and ZnO-WSSe vdW heterostructures. Band spin splitting and Rashba spin splitting are also observed in the band structure of both ZnO-MoSSe and ZnO-WSSe vdW heterostructures. Compared with the PBE calculation, the PBE-SOC band gap values of the ZnO-MoSSe and ZnO-WSSe vdW heterostructures decrease to 1.38 eV and 1.31 eV, respectively. As it is clear from the Table 1, the band gap are larger in HSE06 method as compared to PBE and PBE+SOC. The traditional PBE method is known to underestimate the band gap of semiconductors. The HSE method is often used to correct the gap values. Although the PBE method underestimates the band gap, it is still able to predict the correct trend in band gap variation and to properly demonstrate the physical mechanism, therefore the PBE results can still be expected to be meaningful. One should note that the more accurate HSE band structure can be basically obtained by upshifting/downshifting the CB/VB bands of the PBE bands, indicating the band dispersions given by the PBE functional are still reasonable though the bandgap is too small. Also it shows that the PBE band gap values is larger than the PBE+SOC which is due to the spin splitting of VBM and CBM. Since a local maximum in the VB and/or a local minimum in the CB is known as a valley and the band structure of an ideal valleytronic material is composed of two or more degenerate inequivalent valley states[52].

In Fig. 3(g) we show the spin texture of bands around Γ_v. Three arrows are labeled to designate the spin splitting along uppermost valance band and lower most conduction band. The CB and VB edges are characterized by the degenerate valleys that are marked as λ_{kc}, λ_{kv} and Γ_v. Moreover, first arrow shows the conduction band splitting at the CBM tagged as λ_{kc}, while second shows the valance band splitting at the VBM labelled as λ_{kv}. Third arrow represents the intersection of energy bands indicating the Rashba spin splitting with momentum offset K_R^M and K_R^K around Γ_v rendering Rashba energy E_R^M and E_R^K between M and K symmetry points of Brillion Zone. In Model-I, we can observe that ZnO-MoSSe heterostructure gives an indirect band gap feature, whereas ZnO-WSSe one possesses a direct band gap at K point with semiconducting behavior.

In Model-II, as illustrated in Fig. 3, both the ZnO-MoSSe and ZnO-WSSe heterostructures are featured by the indirect band gap semiconductors with the band gap values of 0.73 eV and 0.95 eV from PBE calculations, respectively, as listed in Table 2. The corresponding VBM and CBM lie at K and M points. HSE06 functional enhanced the band gap values of such heterostructures to 2.1 eV and 2.3 eV, respectively. The spin-orbit interactions substantiate Rashba spin splitting that originates with intersecting bands. The momentum offset KR and the Rashba energy E_R are also indicated. The spin texture of two bands is also correlated with Rashba spin splitting around Γ_{av}. The calculated values of Rashba energy, momentum offset and Rashba energies along Γ, K and M directions respectively due to spin orbit interaction are given in Tabl 3, making the ZnO-Janus MXY heterostructures prominent for valleytornics.

Furthermore, to have a clear picture of the band alignment in

Physical Chemistry Chemical Physics Accepted Manuscript

This journal is © The Royal Society of Chemistry [year]

View Article Online
DOI: 10.1039/D0CP01264E

Published on 20 April 2020. Downloaded by Chalmers Tekniska Hogskola on 4/20/2020 6:31:51 AM.

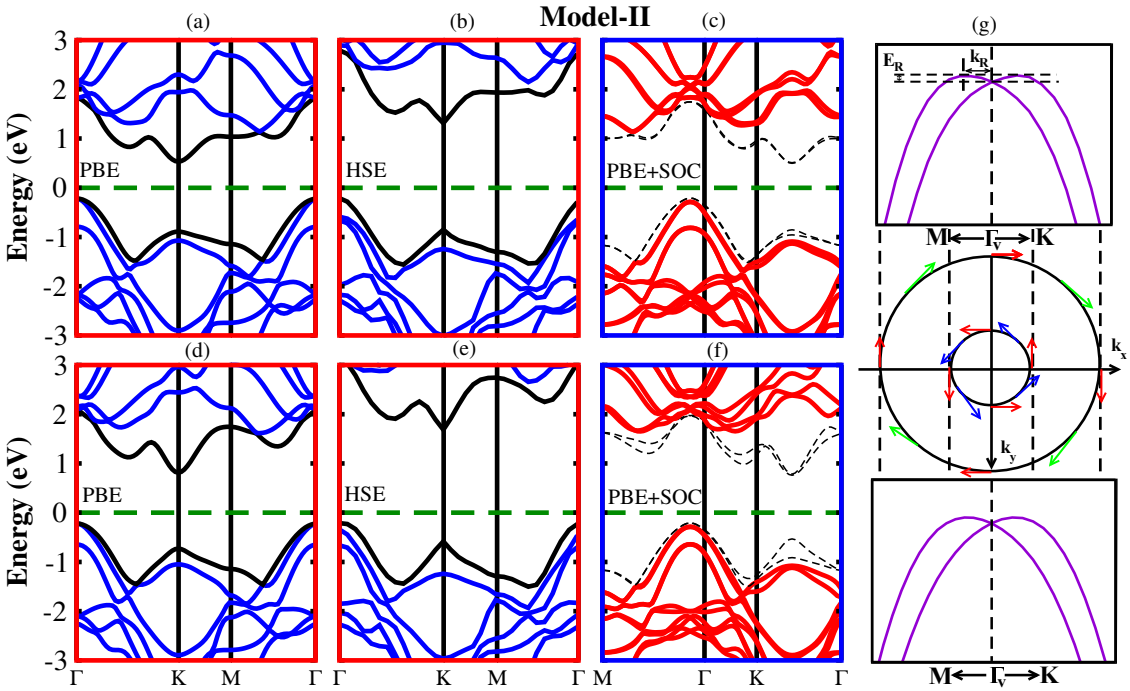

Fig. 4 Model-II: band structure of MoSSe-ZnO (a, b and c) and WSSe-ZnO (d, e and f) van der Waals heterostructures (g) Schematic of spin texture of Rashba Energy (E R K Kand E R M),and momentum offset (K R K and K R M) and Rashba Parameter (Îś R andM)along $\Gamma - K$ and $\Gamma - M$ direction, respectively.

the ZnO-Janus MXY heterostructure, we further calculate their weighted band structures, as depicted in Fig. 4. In the case of the Model-I of ZnO-MoSSe and ZnO-WSSe heterostructure, we can see from Fig. 5(a,b) that both CBM and VBM of the band structures are constituted due to Mo(W)-d_{z^2} orbital, presenting type−I band alignment, thus they are suitable for laser applications[53]. Weighted band structures of ZnO-MoSSe and ZnO-WSSe heterostructures in Model-II indicate type-II band alignment, where the CBM is due to the Mo(W)-d_{z^2} orbital and VBM is dominated by the O-p_z orbital, as depicted in Fig. 5(c,d). Type-II band alignment reveals remarkable applications in optoelectronic and photovoltaic applications due to the efficient electron-hole separation.

The charge density difference is also calculated to understand the underlying mechanism of charge transfer and charge redistribution in the ZnO-Janus MXY heterostructures. The charge density difference is calculated by: $\rho = \rho_{Hetero} - \rho_{ZnO} - \rho_{JanusMXY}$, where ρ_{Hetero}, ρ_{ZnO} and $\rho_{JanusMXY}$ are the charge density of ZnO-Janus MXY heterostructures, ZnO and Janus MXY monolayers, respectively. The charge density difference of the ZnO-MoSSe heterostructure for Model-I and Model-II is visualized in Fig. 5(e) and Fig. 5(f), respectively, in which yellow and red areas correspond to the electron loss and gain, respectively. One can observe that in the ZnO-Janus MXY heterostructures, electrons flowed from ZnO to the Janus MXY layer. It indicates that electrons were donated by the ZnO layer, while the Janus MXY layers accept electrons, resulting to the formation of the *p*-doping in the ZnO monolayer and *n*-doping in Janus MXY layers. Moreover, we can observe that the charges are mainly redistributed between oxygen atoms and adjacent sulfide/selenium layers because of the difference in the electronegativity. Such charge redistribution in the ZnO-Janus MSSe heterostructures creates a built-in electric field, which spatially separates the photogenerated charge carriers. Furthermore, a Bader charge analysis demonstrates that only 0.14 electron/unit cell is transferred from ZnO to MoSSe layers, verifying the weak vdW interaction between ZnO and Janus MXY monolayers.

4 Photocatalytics

In photocatalytic activity, Separation of charge carriers in conduction and valance bands of semiconductor by light illumination induces the redox reaction that ultimately gives the hydrogen and oxygen by splitting water. ZnO has best photocatalytic[36] response and its activity is being checked for its heterostructures with Janus transition metal dichalcogenides. The photocatalytic water splitting for the ZnO, MoSSe and WSSe Janus monolayers and ZnO-Janus vdW heterostructures (Model-I, Model-II) with relative positions of chalcogen atoms on opposite surfaces of transition metal are investigated by using Mulliken electronegativity $E_{VBM} = \chi - E_{elec} + 0.5E_g$ and $E_{CBM} = E_{VBM} - E_g$ for pH = 0/acidic environment.[54,55]. The Fermi level is set at energy of -4.44 eV.

ZnO-Janus vdW heterostructures has suitable band gap for photocatalytic water splitting (see Table II). Also for good photocatalyst response the materials also needs an appropriate band edge positions for the reduction and oxidation potentials. The reduction/oxidation ability could be evaluated by the alignment of CBM and VBM with respect to the water redox potential levels. Fig. 6 shows the band edge alignments of ZnO, Janus monolayers and ZnO-Janus vdW heterostructures with respect to the water reduction and oxidation potential levels at pH = 0. It

Physical Chemistry Chemical Physics Accepted Manuscript

View Article Online
DOI: 10.1039/D0CP01264E

Published on 20 April 2020. Downloaded by Chalmers Tekniska Hogskola on 4/20/2020 6:31:51 AM.

Table 2 Binding energies (E_a, E_b, E_c, E_d, E_e, E_f), inter layer distance (d), Lattice constant (a), bond length ($M-X$), band gap (E_g), work function (ϕ), conduction and valence band edges (eV) of ZnO-Janus heterostructure

Hetrostructures	ZnO-MoSSe		ZnO-WSSe	
Stacking	Model-I	Model-II	Model-I	Model-II
$E_{(a)}$ (eV)	-0.350	-0.399	-0.492	-0.339
h_a (Å)	3.52	3.62	3.52	3.49
$E_{(b)}$ (eV)	-0.389	-0.406	-0.523	-0.344
h_b (Å)	3.60	3.45	3.44	3.42
$E_{(c)}$ (eV)	–0.399	-0.448	-0.541	-0.372
h_c (Å)	3.29	3.41	3.31	3.33
$E_{(d)}$ (eV)	-0.342	-0.389	-0.483	-0.348
h_d (Å)	3.42	3.54	3.58	3.45
$E_{(e)}$ (eV)	-0.370	-0.417	-0.501	-0.347
h_e (Å)	3.35	3.59	3.49	3.43
$E_{(f)}$ (eV)	-0.356	-0.443	-0.530	-0.392
h_f (Å)	3.56	3.50	3.46	3.37
a (Å)	3.27		3.27	
Zn-O (Å)	1.85	1.86	1.85	1.86
Mo-S/Se (Å)	2.42/2.53	2.42/2.53	2.42/2.53	2.42/2.53
W-S/Se (Å)	2.42/2.53	2.42/2.53	2.42/2.53	2.42/2.53
E_g (PBE/PBE-SOC) (eV)	1.40/1.38	0.73/0.68	1.53/1.31	0.95/0.92
E_g (HSE) (eV)	2.00	2.10	2.10	2.30
Φ (eV)	1.18	1.07	1.27	1.06
E_{VB} (pH = 0) (eV)	1.94	1.99	2.10	2.20
E_{CB} (pH = 0) (eV)	-0.058	-0.108	0.001	-0.101
E_{VB} (pH = 7) (eV)	1.527	1.577	1.687	1.787
E_{CB} (pH = 7) (eV)	-0.471	-0.521	-0.412	-0.514
E_{VB} (pH = 14) (eV)	1.116	1.274	1.166	1.374
E_{CB} (pH = 14) (eV)	-0.884	-0.825	-0.934	-0.925

Table 3 Rashba Energy (E_R^K and E_R^M in meV), momentum offset (k_R^K and k_R^M in Å^{-1}, and Rashba Parameter (α_R^K and α_R^M in eV) along $\Gamma-K$ and $\Gamma-M$ directions respectively.

Types	Heterostructures	Methods	E_R^K	k_R^K	α_R^K	E_R^M	k_R^M	α_R^M
Model-I	ZnO-MoSSe	PBE-SOC	0.030	1.401	0.041	0.089	1.071	0.170
	ZnO-WSSe	PBE-SOC	0.003	0.601	0.010	0.502	1.201	0.830
Model-II	ZnO-MoSSe	PBE-SOC	0.011	1.701	0.003	0.702	1.601	0.875
	ZnO-WSSe	PBE-SOC	0.002	1.201	0.003	0.601	1.501	0.802

can be clearly seen that both CB and VB edges of MoSSe, WSSe and ZnO monolayers are located more negative and more positive than the redox potential of H^+/H_2 and O_2/H_2O, respectively, which shows good response for photocatalyst activities also in good agreement with previous works[38,56,57]. In ZnO-MoSSe and ZnO-WSSe heterostructures (Model-I) shows that the level of CB and VB is higher than that of standard redox potentials. These energy levels are sufficient for electrons and holes to dissociate water into H^+/H_2 and O_2/H_2O, which makes ZnO-MoSSe and ZnO-WSSe heterostructures (Model-I) good photocatalytic activities. Fig 6. also shows that ZnO-MoSSe (Model-II), the VB edge straddles the oxidation potential while the CB edge is signicantly lower than the reduction potential and thus fails to reduce water into H^+/H_2. While ZnO-WSSe heterostructures (Model-II) shows good response for photocatalytic. Compeering both models that model-I sows good photocatalytic response then model-II due to the relative order of chalcogen atoms in janus monolayers by vdW stacking with ZnO monolayer. A similar trend is also demonstrated for GeC-MSSe (M=Mo, W) van der Waals heterostructures[38]. As most of reduction and oxidation involve in aqueous solution, which are closely correlated with acid (pH = 0) and base (pH = 7) properties. We already addressed the performance of ZnO-Janus heterostructure for acid environment, which shows good response. Now to check these heterostructures for base (pH = 7), we used the Nernst equation[58–60], which is E_{pH} = 0 - 0.059 × pH. The values obtained for pH = 7 are also given in Tab. 2, which also conform that these all heterostructures shows good response for basic environment. Using this equation, we can obtain the redox potentials of H^+/H_2 and H_2O/O_2 for any pH. As the pH value increases from 0 to 14, the corresponding redox potentials (H^+/H_2 and H_2O/O_2) will shift upward. All these results are listed in Table. 2. In this process for conversion of solar

Physical Chemistry Chemical Physics Accepted Manuscript

This journal is © The Royal Society of Chemistry [year]

View Article Online
DOI: 10.1039/D0CP01264E

Published on 20 April 2020. Downloaded by Chalmers Tekniska Hogskola on 4/20/2020 6:31:51 AM.

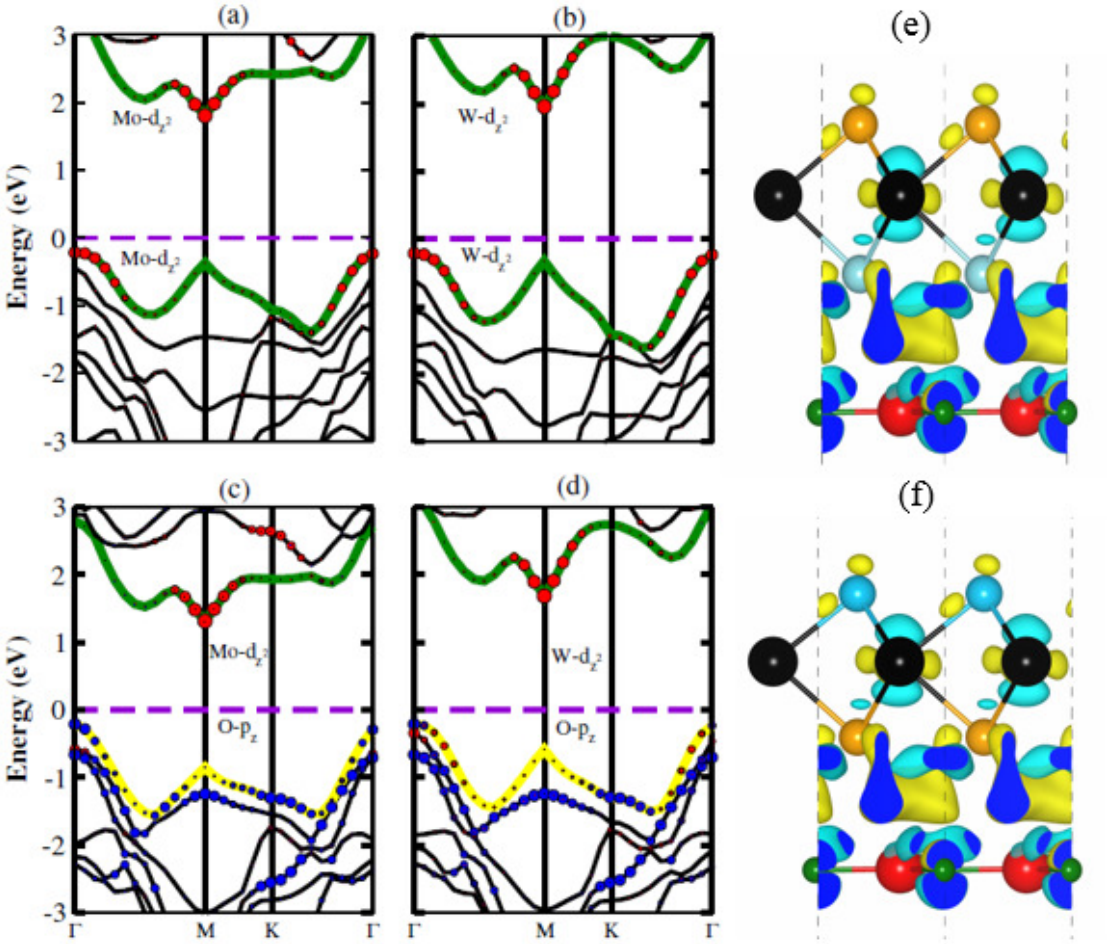

Fig. 5 Weighted band structure: Model-I (a) MoSSe-ZnO, (b) WSSe-ZnO, Model-II (c) MoSSe-ZnO, (d) WSSe-ZnO. The green and blue lines represent the Mo(W)-d_{z^2} and O-p_z orbitals, respectively. Schematic of charge density difference (with isovalue 0.00025 e/Bohr^3 for MoSSe-ZnO heterostructure in both Model-I (e) and Model-II (f), respectively.

light into hydrogen, is an attractive technique for the production of clean and renewable energy device applications[61].

5 Conclusion

In summary, we have investigated systematically ZnO-Janus heterostructure in detail,such as the lectronic properties, charge density difference, work function, band alignment and photocatalytic roperties using first-principles calculations. Two different possible models of ZnO-Janus heterostructures are presented with alternative order of chalcogen atoms at opposite surfaces in janus. The most favorable stacking pattern of both models is dynamically and energetically feasible by finding the thermal stabilities and binding energies of ZnO-Janus heterostuctures. We find that the band structures of ZnO-MoSSe and ZnO-WSSe is indarct band gap for both models while model-I shows type-I and model-II shows type-II band alignment respectively. In particular, a greater Rashba spin polarization is demonstrated in ZnO-WSSe in model-I from other heterostructures. Inter layer charge transfer shows that the electron are transfer from ZnO to Janus monolayers. Furthermore, valence(conduction) band edge potentials are calculated to understand the photocatalytic behavior of these systems. Energetically favourable band edge positions in ZnO-Janus heterostucturs make them suitable for water splitting at zero pH. We found that the ZnO-Janus heterostructure are promising candidates for water splitting with conduction and valence band edges positioned just outside of the redox interval. In comparison to Model-I and Model-II, the ZnO-MoSSe heterostructure possesses the strongest reduction power and ZnO-WSSe heterostructure possesses the strongest oxidation power locating in Model-I.

Conflicts of interest

The authors declare that there are no conflicts of interest regarding the publication of this paper.

Acknowledgements

This research is supported by the Higher Education Commission of Pakistan (HEC) under Project No. 5727/261 KPK/NRPU/R&D/HEC2016 and Vietnam National Foundation for Science and Technology Development (NAFOSTED) under grant number 103.01-2019.05.

References

1 T. N. Veziroğlu, S. Şahi *et al.*, *Energy Convers. Manag.*, 2008, **49**, 1820–1831.

Physical Chemistry Chemical Physics Accepted Manuscript

View Article Online
DOI: 10.1039/D0CP01264E

Published on 20 April 2020. Downloaded by Chalmers Tekniska Hogskola on 4/20/2020 6:31:51 AM.

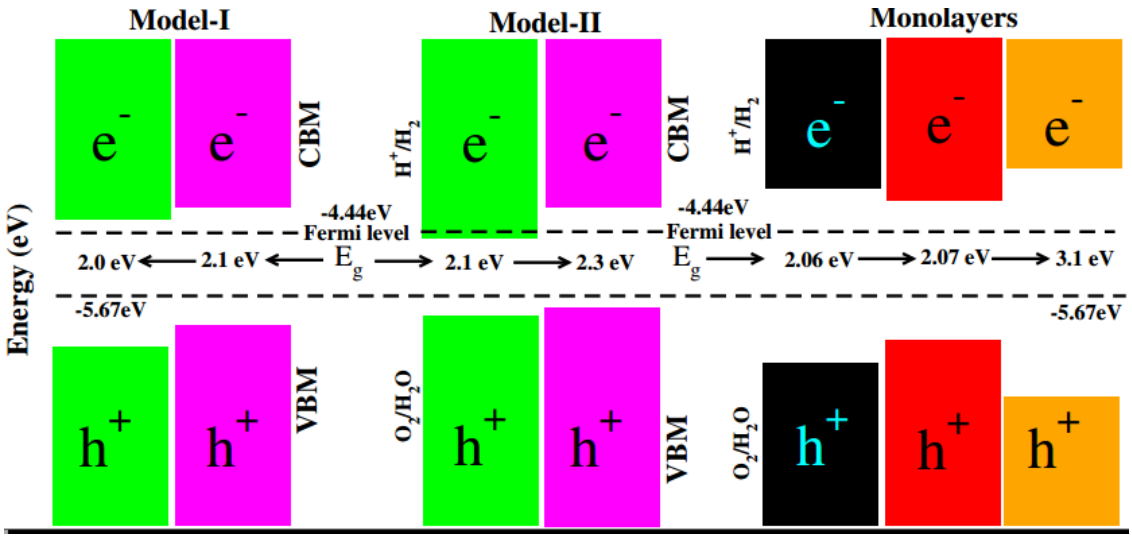

Fig. 6 Valence band (VB) and conduction band (CB) edge alignment of Model-I, -II van der Waals heterostructures and corresponding MoSSe, WSSe and ZnO monolayers. The standard oxidation (-5.67 eV) and reduction (-4.44 eV) potentials for water splitting into O_2/H_2O and H^+/H_2, respectively.

2 M. Balat, *Int. J. Hydrog. Energy*, 2008, **33**, 4013–4029.
3 J.-C. Martin, P. Millington, B. Campbell, L. Barron and S. Fisher, *Int. J. Hydrog. Energy*, 2019, **44**, 12880–12889.
4 P. P. Edwards, V. L. Kuznetsov, W. I. David and N. P. Brandon, *Energy Policy*, 2008, **36**, 4356–4362.
5 S. I. Ngo, Y.-I. Lim, W. Kim, D. J. Seo and W. L. Yoon, *Appl. Energy*, 2019, **236**, 340–353.
6 A. Fujishima and K. Honda, *Nature*, 1972, **238**, 37–38.
7 F. E. Osterloh, *Chem. Mater.*, 2007, **20**, 35–54.
8 X. Hu, G. Li and J. C. Yu, *Langmuir*, 2009, **26**, 3031–3039.
9 C. Chowdhury, S. Karmakar and A. Datta, *J. Phys. Chem. C*, 2017, **121**, 7615–7624.
10 M. Matsuoka, M. Kitano, M. Takeuchi, K. Tsujimaru, M. Anpo and J. M. Thomas, *Catalysis Today*, 2007, **122**, 51–61.
11 V. Artero, M. Chavarot-Kerlidou and M. Fontecave, *Angew Chem. Int. Ed.*, 2011, **50**, 7238–7266.
12 D. Deng, K. Novoselov, Q. Fu, N. Zheng, Z. Tian and X. Bao, *Nat. Nanotechnol.*, 2016, **11**, 218.
13 E. Pomerantseva and Y. Gogotsi, *Nat. Energy*, 2017, **2**, 17089.
14 A. Bafekry, C. Stampfl, S. F. Shayesteh and F. Peeters, *Adv. Elec. Mater.*, 2019, **5**, 1900459.
15 J. Ge, Y. Zhang, Y.-J. Heo and S.-J. Park, *Catalysts*, 2019, **9**, 122.
16 K. Ren, M. Sun, Y. Luo, S. Wang, J. Yu and W. Tang, *Appl. Surf. Sci.*, 2019, **476**, 70–75.
17 A. Bafekry, C. Stampfl and S. Farjami Shayesteh, *ChemPhysChem*, 2019, **21**, 164–174.
18 A. Bafekry, S. Farjami Shayesteh, M. Ghergherehchi and F. M. Peeters, *J. Appl. Phys.*, 2019, **126**, 144304.
19 A. Bafekry, S. F. Shayesteh and F. M. Peeters, *J. Appl. Phys.*, 2019, **126**, 215104.
20 Q.-F. Yao, J. Cai, W.-Y. Tong, S.-J. Gong, J.-Q. Wang, X. Wan, C.-G. Duan and J. Chu, *Phys. Rev. B*, 2017, **95**, 165401.
21 A. Bafekry, C. Stampfl, M. Ghergherehchi and S. F. Shayesteh, *Carbon*, 2020, **157**, 371–384.
22 A. Bafekry, *Physica E*, 2020, **118**, 113850.
23 M. Zhang, X.-X. Wang, W.-Q. Cao, J. Yuan and M.-S. Cao, *Adv. Opt. Mater.*, 2019, **7**, 1900689.
24 H. Guo, N. Lu, L. Wang, X. Wu and X. C. Zeng, *J. Phys. Chem. C*, 2014, **118**, 7242–7249.
25 A. Chernikov, T. C. Berkelbach, H. M. Hill, A. Rigosi, Y. Li, O. B. Aslan, D. R. Reichman, M. S. Hybertsen and T. F. Heinz, *Phys. Rev. Lett.*, 2014, **113**, 076802.
26 N. Zibouche, P. Philipsen and A. Kuc, *J. Phys. Chem. C*, 2019, **123**, 3892–3899.
27 B. Amin, T. P. Kaloni and U. Schwingenschlögl, *Rsc Adv.*, 2014, **4**, 34561–34565.
28 B. Amin, N. Singh and U. Schwingenschlögl, *Phys. Rev. B*, 2015, **92**, 075439.
29 A. Bafekry and M. Neek-Amal, *Phys. Rev. B*, 2020, **101**, 085417.
30 A. Bafekry, B. Akgenc, S. F. Shayesteh and B. Mortazavi, *Appl. Surf. Sci.*, 2020, **505**, 144450.
31 T. Roy, M. Tosun, X. Cao, H. Fang, D.-H. Lien, P. Zhao, Y.-Z. Chen, Y.-L. Chueh, J. Guo and A. Javey, *ACS Nano*, 2015, **9**, 2071–2079.
32 O. Lopez-Sanchez, E. Alarcon Llado, V. Koman, A. Fontcuberta i Morral, A. Radenovic and A. Kis, *Acs Nano*, 2014, **8**, 3042–3048.
33 R. Zhang, B. Li and J. Yang, *Nanoscale*, 2015, **7**, 14062–14070.
34 F. Li, W. Wei, P. Zhao, B. Huang and Y. Dai, *J. Phys. Chem. Lett.*, 2017, **8**, 5959–5965.
35 C. Xia, W. Xiong, J. Du, T. Wang, Y. Peng and J. Li, *Phys. Rev. B*, 2018, **98**, 165424.
36 P. V. Radovanovic, N. S. Norberg, K. E. McNally and D. R. Gamelin, *J. Am. Chem. Soc.*, 2002, **124**, 15192–15193.
37 X. Ji, J. Song, T. Wu, Y. Tian, B. Han, X. Liu, H. Wang, Y. Gui,

Physical Chemistry Chemical Physics Accepted Manuscript

This journal is © The Royal Society of Chemistry [year]

View Article Online
DOI: 10.1039/D0CP01264E

Published on 20 April 2020. Downloaded by Chalmers Tekniska Hogskola on 4/20/2020 6:31:51 AM.

Physical Chemistry Chemical Physics Accepted Manuscript

Y. Ding and Y. Wang, *Sol. Energy Mater. Sol. Cells*, 2019, **190**, 6–11.

38 H. U. Din, M. Idrees, A. Albar, M. Shafiq, I. Ahmad, C. V. Nguyen and B. Amin, *Phys. Rev. B*, 2019, **100**, 165425.

39 K. D. Pham, N. N. Hieu, H. V. Phuc, B. D. Hoi, V. V. Ilysov, B. Amin and C. V. Nguyen, *Comput. Mater. Sci.*, 2018, **153**, 438–444.

40 L. S. Cavalcante, M. N. Gjerding, A. Chaves and K. S. Thygesen, *J. Phys. Chem. C*, 2019, **123**, 16373–16379.

41 D. Xu, B. Zhai, Q. Gao, T. Wang, J. Li and C. Xia, *J. Phys. D: Appl. Phys.*, 2019, **53**, 055104.

42 W. Yin, B. Wen, Q. Ge, D. Zou, Y. Xu, M. Liu, X. Wei, M. Chen and X. Fan, *Prog. Nat. Sci.*, 2019, **29**, 335–340.

43 W. Kohn and L. J. Sham, *Phys. Rev.*, 1965, **140**, A1133–A1138.

44 G. Kresse and J. Hafner, *Phys. Rev. B*, 1993, **47**, 558.

45 G. Kresse and J. Furthmüller, *Phys. Rev. B*, 1996, **54**, 11169.

46 J. P. Perdew, K. Burke and M. Ernzerhof, *Phys. Rev. Lett.*, 1996, **77**, 3865.

47 S. Grimme, *J. Comput. Chem.*, 2006, **27**, 1787–1799.

48 J. Heyd, G. E. Scuseria and M. Ernzerhof, *J. Chem. Phys.*, 2003, **118**, 8207–8215.

49 R. Yuan, J. A. Napoli, C. Yan, O. Marsalek, T. E. Markland and M. D. Fayer, *âĂŐACS Cent. Sci.*, 2019, **5**, 1269–1277.

50 M. Idrees, H. Din, R. Ali, G. Rehman, T. Hussain, C. Nguyen, I. Ahmad and B. Amin, *Phys. Chem. Chem. Phys.*, 2019, **21**, 18612–18621.

51 H. Din, M. Idrees, T. A. Alrebdi, C. V. Nguyen and B. Amin, *Comput. Mater. Sci.*, 2019, **164**, 166–170.

52 J. R. Schaibley, H. Yu, G. Clark, P. Rivera, J. S. Ross, K. L. Seyler, W. Yao and X. Xu, *Nat. Rev. Mater.*, 2016, **1**, 16055.

53 M. Hetterich, M. Dawson, A. Y. Egorov, D. Bernklau and H. Riechert, *Appl. Phys. Lett.*, 2000, **76**, 1030–1032.

54 J. Liu, X. Fu, S. Chen and Y. Zhu, *Appl. Phys. Lett.*, 2011, **99**, 191903.

55 H. L. Zhuang and R. G. Hennig, *Phys. Rev. B*, 2013, **88**, 115314.

56 X. Ma, X. Wu, H. Wang and Y. Wang, *J. Mater. Chem. A*, 2018, **6**, 2295–2301.

57 Y. Ji, M. Yang, H. Lin, T. Hou, L. Wang, Y. Li and S.-T. Lee, *J. Phys. Chem. C*, 2018, **122**, 3123–3129.

58 J. M. Bolts and M. S. Wrighton, *J. Phys. Chem.*, 1976, **80**, 2641–2645.

59 T. A. Pham, D. Lee, E. Schwegler and G. Galli, *J. Am. Chem. Soc.*, 2014, **136**, 17071–17077.

60 X. Li, J. Yu, J. Low, Y. Fang, J. Xiao and X. Chen, *J. Mater. Chem. A*, 2015, **3**, 2485–2534.

61 V. Chakrapani, J. C. Angus, A. B. Anderson, S. D. Wolter, B. R. Stoner and G. U. Sumanasekera, *Science*, 2007, **318**, 1424–1430.